SINTECHCOM: Science, Technology and Communication Journal
Vol. 2, No. 1, October 2021, pp. 21-28, DOI: 10.59190/stc.v2i1.209

# Microwave media simulation to generate nitrogen plasma at atmospheric pressure

**Muhammad Fauzan*, Reeky Fardinata, Khaikal Ramadhan**
Department of Physics, Universitas Riau, Pekanbaru 28293, Indonesia

**ABSTRACT**

The development of methods to generate artificial plasma continues to be carried out for industrial purposes in machines and production products. To overcome experimental problems in modeling development, various methods have been carried out. One of the methods used is to simulate the air in a microwave oven. This simulation will describe the electric field distribution of each mode to identify the plasma by introducing the cutoff frequency. Ionization gas with a composition of 78% Nitrogen, 21% Oxygen, and 1% other gases at a pressure of 1 atm. The microwave oven chamber is made of an iron conductor in the form of a beam with dimensions 29 × 29 × 19 $cm^3$, with a continuous supply of 800 W and 220 V. Power loss as a function of frequency shows the cutoff frequency using an S-parameter graph and electric field distribution as a function of position in each mode. The plasma formed is in modes 20, 01, and 11 because the electric field exceeds the breakdown voltage value to generate plasma, which is 6 × $10^6$ V/m. The bigger the electric field, the more plasma is produced, which is indicated in the mode positions in the microwave oven.

**ARTICLE INFO**

**Article history:**

Received Oct 14, 2021
Revised Oct 23, 2021
Accepted Oct 26, 2021

**Keywords:**

Cutoff Frequency
Electric Field
Microwave
Nitrogen Plasma
Transverse Electrical



* **Corresponding Author**
E-mail address: mhdfzn11@gmail.com

## 1. INTRODUCTION

The abundance of plasma in nature makes researchers carry out various kinds of research to develop it to be useful for every aspect of human life [1]. One of the efforts made is to generate artificial plasma in the laboratory [2, 3]. The generation process can be carried out by heating the gas in a closed space in the microwave oven so that ionization occurs [4]. Ionization occurs as a result of increasing the electric field in the microwave oven space [5, 6]. An electric field that exceeds the breakdown voltage of 6 × $10^6$ V/m will produce plasma [7]. The interaction of microwaves in a microwave oven chamber is similar to the interaction of visible light on a mirror [8, 9]. Microwaves that come will be reflected to form a standing wave [10]. In general, these interactions can be explained through Maxwell's constitutive equations which provide a relationship between Maxwell's equations and the medium of propagation [11, 12]. Maxwell's constitutive equations can also be used to determine the electric transverse in a conductor medium in the form of a beam [13]. These equations form the Helmholtz equation in the form of [14]:

$$\left(\frac{\partial^2}{\partial x^2}+\frac{\partial^2}{\partial y^2}+k^2\right)h_z(x,y)=0 \quad (1)$$

Equation (1) can be solved by using the variable separation method to get the solution, namely:

$$E_x=\frac{j\omega\mu n\pi}{k^2 b}A_{mn}cos\frac{m\pi x}{a}sin\frac{n\pi y}{b}e^{-j\beta z} \quad (2)$$

$$E_y = \frac{-j\omega\mu m\pi}{k^2 a} A_{mn} sin\frac{m\pi x}{a} cos\frac{n\pi y}{b} e^{-j\beta z} \quad (3)$$

$$H_x = \frac{j\beta m\pi}{k^2 a} A_{mn} sin\frac{m\pi x}{a} cos\frac{n\pi y}{b} e^{-j\beta z} \quad (4)$$

$$H_y = \frac{j\beta n\pi}{k^2 b} A_{mn} cos\frac{m\pi x}{a} sin\frac{n\pi y}{b} e^{-j\beta z} \quad (5)$$

Equations (2) to (5) will give the electric field distribution in the space inside the microwave oven [15]. In a microwave oven, the distribution of the electric field formed is also determined from the transverse electric mode which can propagate based on its cutoff frequency [16-19]. The cutoff frequency is defined as the minimum frequency required by microwaves to propagate in the microwave oven, which is formulated as [20]:

$$f_c = \frac{1}{2\pi\sqrt{\mu\varepsilon}} \sqrt{\left(\frac{m\pi}{a}\right)^2 + \left(\frac{n\pi}{b}\right)^2} \quad (6)$$

The focus of this research is to simulate the air in the microwave oven using the high-frequency structured simulator (HFSS) software with a frequency of 0.915 GHz to 2.45 GHz so that it reaches the ionization state. An analysis of the cutoff frequency is carried out to obtain the type of mode that can propagate so that the distribution of the electric field of each mode to the microwave oven space can be displayed. The plasma formed can be identified through the distribution of the electric field in each mode so that it can be seen which type of mode has the most influence on plasma formation.

## 2. PLASMA GENERATOR MODEL

The identified gas is air which consists of 78% nitrogen, 21% oxygen, and 1% other gases [21-23]. At atmospheric pressure, the number of nitrogen gas molecules is $2.4 \times 10^{25}$ molecules obtained through the ideal gas equation [24, 25]. The gas will be ionized using microwaves in an enclosed space in the form of a block at a state of 1 atm. Microwaves are generated through a magnetron with a frequency range of 1 – 30 GHz and a power of 800 W. The microwaves are then forwarded to a waveguide with dimensions $a$ = 2.286 cm and $b$ = 1.016 cm to determine the frequency that can propagate in the microwave space with an operating frequency limit of 17 GHz on the waveguide. The frequency that resonates in the microwave oven to generate plasma ranges from 0.915 to 2.45 GHz. This is done because only certain frequencies can interact with the plasma.

The simulation step is carried out by designing the geometry of the space in the microwave oven in the form of a beam with dimensions $(29 \times 29 \times 19)$ cm$^3$. The space is made of iron material which is a conductor. The direction of wave propagation in the material is set using the wave port menu in HFSS. Then set the resonant frequency in the oven with a range of 0.915 – 2.45 GHz and a step size of 0.01 GHz to display the distribution of the electric field in the microwave oven.

To determine the cutoff frequency and electric field, it is done by entering parameters such as the operating frequency on the waveguide of 17 GHz, the initial frequency of the magnetron of 1 – 30 GHz, and the power supply is 800 W so that the electric field and the type of propagating mode can be seen. Validation is carried out on the cutoff frequency by comparing the simulation data with reference data.

## 3. ELECTRIC FIELD DISTRIBUTION ANALYSIS

The result of reflection on natural white color pearl in Figure 2 shows that it reflects most of the visible color at wavelength 400 nm, 450 – 470 nm, 550 nm, 600 – 630 nm, and 665 nm which represent all color possesses by visible spectrum, which are violet, indigo, green, yellow, orange, and red. Therefore this result shows that all those reflective colors are then superimposed and combined to become one bright white color.

Figure 1 shows the cutoff frequency of transverse electrical (TE) of $TE_{10}$ at 6.58 GHz, $TE_{20}$ at 13.19 GHz, $TE_{01}$ at 14.81 GHz, and $TE_{11}$ at 16.22 GHz. Figure 2 is also known as an S-parameter

graph which has a power loss function (dB) against a frequency function (GHz). In electromagnetic waves, the power loss can be interpreted as a decrease in the intensity of the wave radiation due to absorption and scattering. As a result, the energy to propagate will be reduced so that the range will be reduced. In Figure 2 it can be seen that for $TE_{10}$, $TE_{20}$, $TE_{01}$, and $TE_{11}$ each requires a frequency of 6.58 GHz, 13.19 GHz, 14.81 GHz, and 16.22 GHz to suppress energy reduction due to absorption and scattering. Based on equation 6 the cutoff frequency value is determined from the type of mode (mn) and the waveguide dimension value. The results obtained are slightly different from those carried out by Van Compernolle et al. (2015) [2]. The comparison of the results obtained can be seen in Table 1 below.

Table 1. Comparison of simulated cutoff frequency with reference.

| m | n | Simulation $f_c$ (GHz) | Refernces $f_c$ (GHz) |
|---|---|---|---|
| 1 | 0 | 6.58 | 6.56 |
| 2 | 0 | 13.19 | 13.12 |
| 0 | 1 | 14.81 | 14.76 |
| 1 | 1 | 16.22 | 16.15 |

From Table 1 it can be seen that $TE_{10}$ has the lowest cutoff frequency. This is because in the case of $TE_{10}$ the value of b in the cutoff frequency equation can be ignored, so that the cutoff frequency at $TE_{10}$ can be defined as:

$$f_c = \frac{c}{2a} \tag{7}$$

Equation (7) can also be interpreted that $TE_{10}$ has the largest cutoff wavelength compared to other modes so that $TE_{10}$ is also called the most dominant mode.

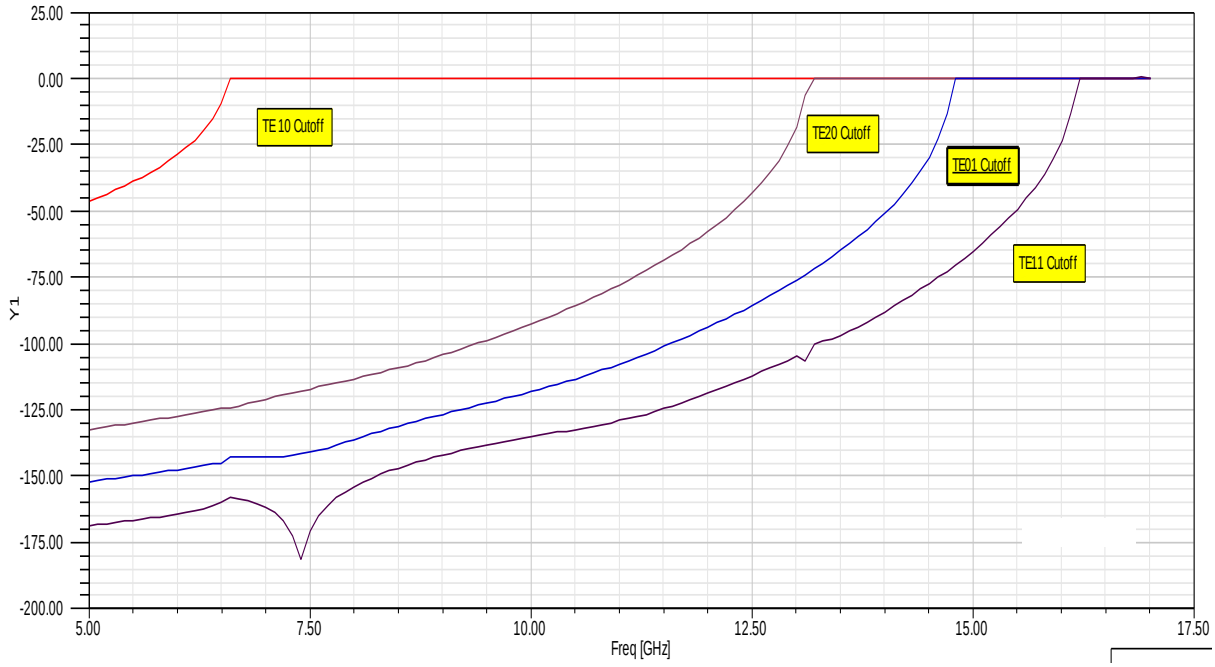


Figure 1. Cutoff frequency graph.

In Figure 1 there are only four types of TE modes that propagate, namely $TE_{10}$, $TE_{20}$, $TE_{01}$, and $TE_{11}$ because they have a cutoff frequency that does not exceed the operating frequency limit (17 GHz). Other modes that have a cutoff frequency above 17 GHz will be cutoff. In Figure 1 it only has TE mode. TM mode in this case cannot propagate because it has a cutoff frequency that exceeds the operating frequency.

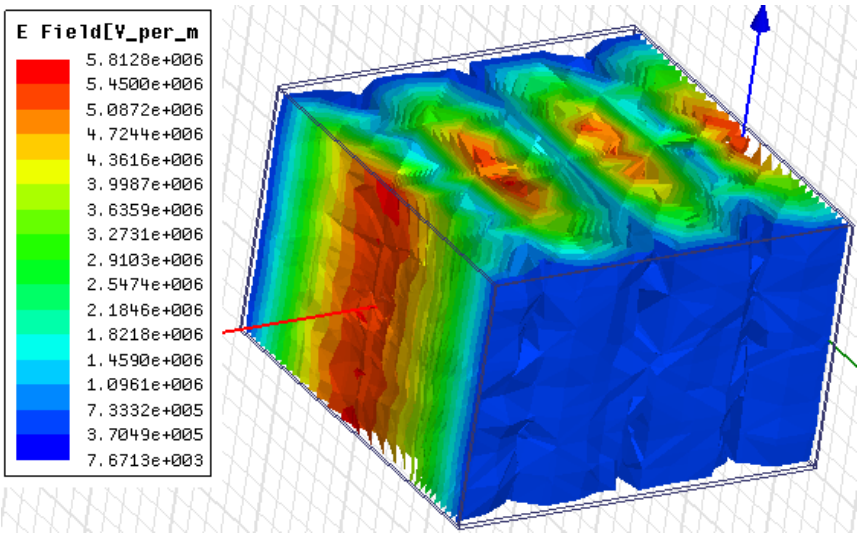


Figure 2. Electric field distribution on $TE_{10}$.

Figure 2 is the distribution of the $TE_{10}$ electric field at a cutoff frequency of 6.58 GHz. The wave on $TE_{10}$ forms a standing wave which has three nodes and three antinodes with the direction of propagation perpendicular to the z-axis. It can be seen that the highest electric field value is at each antinode with a value of $5.81 \times 10^6$ V/m. This shows that in $TE_{10}$ the gas has not yet experienced ionization because for gas ionization to occur it requires a minimum electric field of $6 \times 10^6$ V/m. The lowest electric field is in the node region with a value of $7.63 \times 10^3$ V/m. The average electric field value at $TE_{10}$ is $2.91 \times 10^6$ V/m.

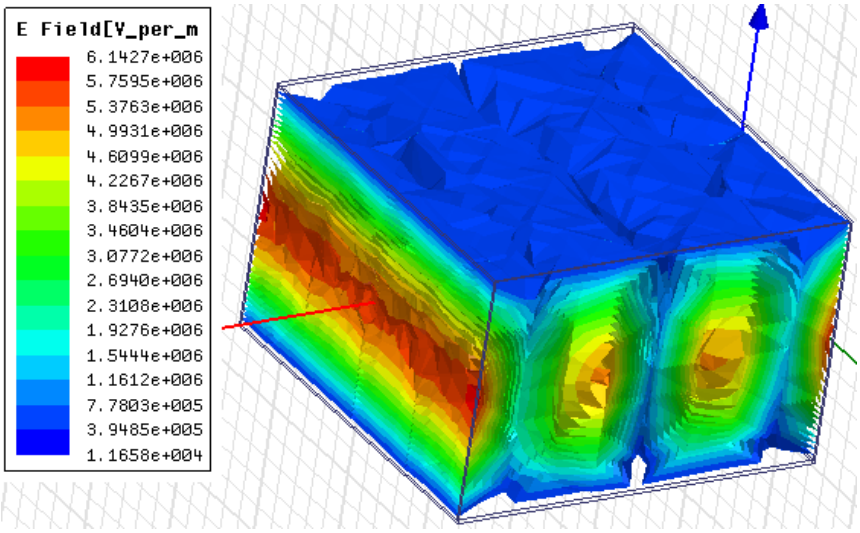


Figure 3. Electric field distribution on $TE_{20}$.

Figure 3 is the distribution of the $TE_{20}$ electric field at a cutoff frequency of 13.19 GHz. The wave on $TE_{20}$ forms a standing wave that has three antinodes and three nodes with the direction of propagation parallel to the z-axis. The highest electric field at $TE_{20}$ is in the antinode region with a value of $6.14 \times 10^6$ V/m. In $TE_{20}$ the gas is ionized due to the electric field that exceeds the minimum limit to ionize the gas. The ionization that occurs in this gas indicates the formation of plasma at $TE_{20}$. The lowest electric field value in this mode is in the node region with a value of $1.16 \times 10^4$ V/m and the average electric field of $3.08 \times 10^6$ V/m.

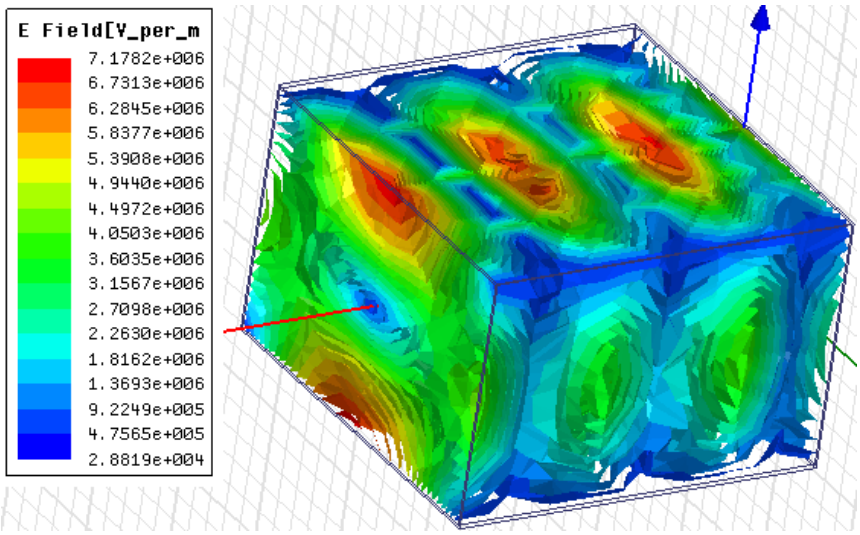


Figure 4. Electric field distribution on $TE_{01}$.

Figure 4 is the distribution of the $TE_{01}$ electric field at a cutoff frequency of 14.81 GHz. The wave on $TE_{01}$ forms a standing wave which has two antinodes and two nodes with the direction of propagation parallel to the z-axis direction. The highest electric field is in the antinode region with a value of $7.18 \times 10^6$ V/m. In $TE_{01}$, the gas also undergoes an ionization process because the electric field exceeds the minimum electric field limit to ionize the gas. This ionization process indicates the formation of plasma in the region that has an electric field value that exceeds the minimum limit, especially in the antinode region. The lowest electric field is in the node region with a value of $2.88 \times 10^4$ V/m and the average electric field at TE01 is $3.62 \times 10^6$ V/m.

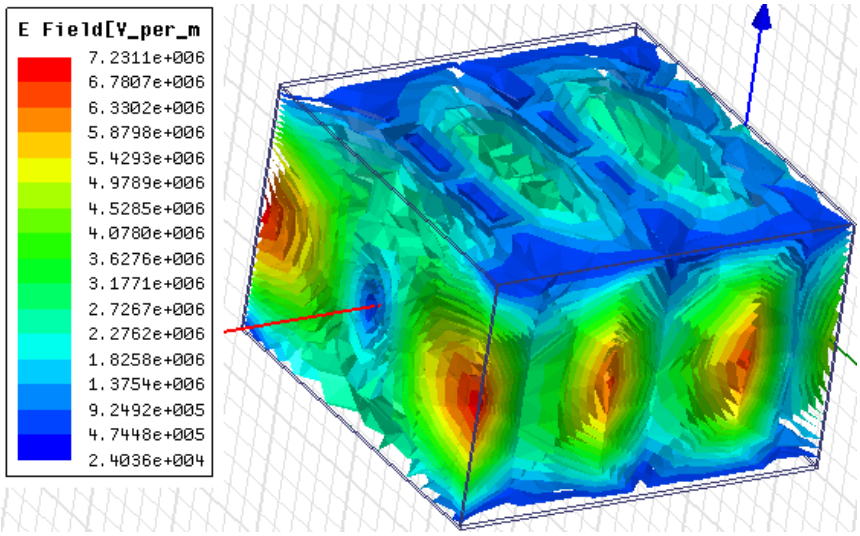


Figure 5. Electric field distribution on $TE_{11}$.

Figure 5 is the distribution of the $TE_{11}$ electric field at a cutoff frequency of 16.22 GHz. The wave on $TE_{11}$ forms a standing wave which has three antinodes and three nodes with the direction of propagation parallel to the z-axis direction. Same as the previous three modes, the highest electric field is in the antinode region with a value of $7.23 \times 10^6$ V/m and the lowest electric field is in the node region with a value of $2.4 \times 10^4$ V/ m. The electric field in $TE_{11}$ has the largest value compared to the previous three modes. In this mode the gas also undergoes ionization which indicates the formation of plasma in the area around the antinode. Because it has a higher electric field value than the other three modes, more plasma is formed than the other modes. The average electric field at $TE_{11}$ is $3.63 \times 10^6$ V/m.

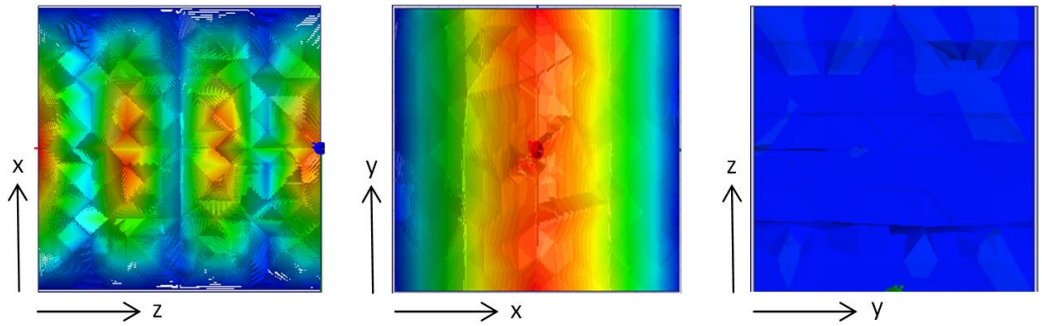


Figure 6. The standing wave pattern formed by $TE_{10}$.

Figure 6 is a standing wave pattern formed at $TE_{10}$. The xz plane shows a pattern forming three peaks (antinodes) with a periodic distance of 9.6 cm from each peak. because of its periodic nature, the notation of the distance between the peaks in the xz plane can be written as 0 cm, 9.6 cm, 19.2 cm, and 28.8 cm. No plasma is formed at any of these peaks because the electric field is not sufficient to ionize the gas. No pattern is formed in the yz plane because the standing wave propagates perpendicular to the z-axis direction.

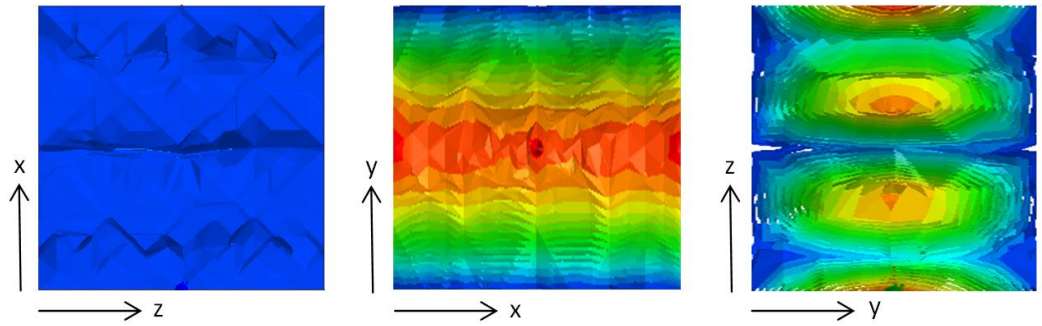


Figure 7. The standing wave pattern formed by $TE_{20}$.

Figure 7 is a standing wave pattern formed by $TE_{20}$ in the xy, xz and yz planes. The standing wave pattern in the xy plane is transverse along the x axis. No standing wave pattern is formed in the xz plane. The standing wave formed in the yz plane has three peaks with a periodic distance between the peaks of 9.3cm. In Figure 3 it can be seen that the peak area is ionized which indicates the formation of plasma in that area. The position of the plasma in the peak region along the z-axis can be estimated to be at a distance of 0 cm, 9.6 cm, and 19.2 cm.

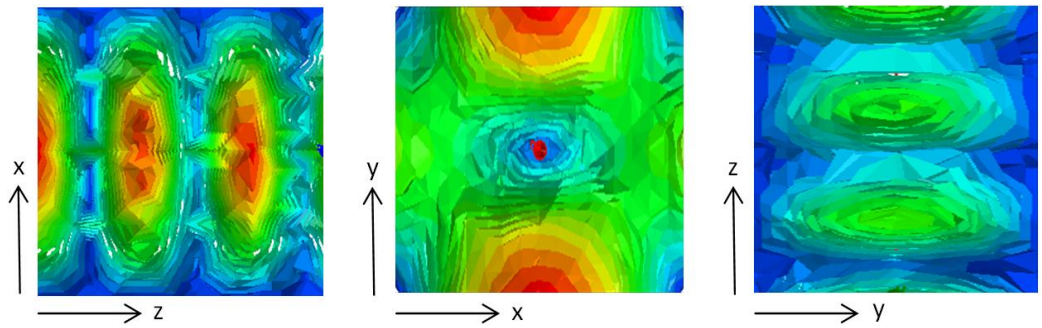


Figure 8. The standing wave pattern formed by $TE_{01}$.

Figure 8 is a standing wave pattern formed by $TE_{01}$ in the xy, xz and yz planes. The pattern formed in the xy plane appears to be plasma forming at the bottom and top of the plane. The standing wave pattern formed in the xz plane has two perfect peaks and one-half peak with a periodic distance

between peaks of 9.6 cm. Based on Figure 4 the area around the peak undergoes an ionization process to form plasma. The plasma producing area is at a distance of 0 cm, 9.6 cm, and 19.2 cm. The standing wave pattern in the yz plane does not have enough energy to generate plasma.

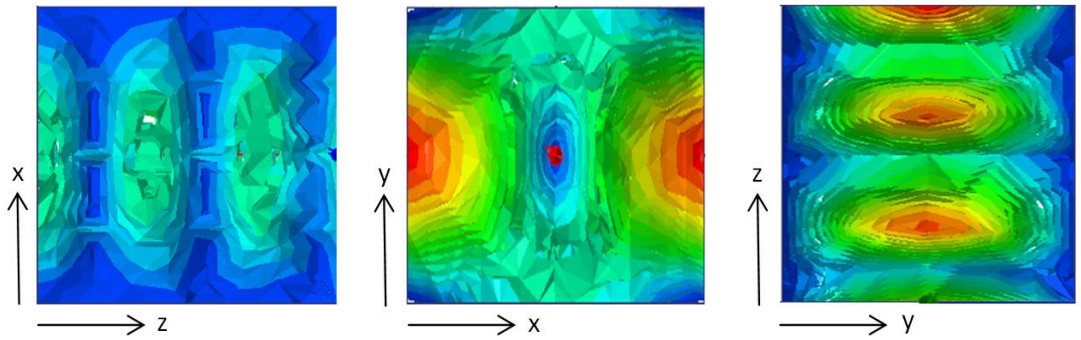


Figure 9. The standing wave pattern formed by $TE_{11}$.

Figure 9 is a standing wave pattern formed by $TE_{11}$ in the xy, xz and yz planes. The standing wave pattern formed in the xy plane with the plasma produced on the right and left of the plane. The standing wave pattern formed in the xz plane does not have enough energy to generate plasma. The standing wave pattern formed in the yz plane. The pattern has two perfect peaks and a half peak with a periodic distance between the peaks of 9.6 cm. $TE_{11}$ experienced the highest ionization so that a lot of plasma was produced in the peak region. The position of the plasma formed at the crest of the wave in the yz plane is at a distance of 0 cm, 9.6 cm, and 19.2 cm.

## 4. CONCLUSION

Based on the results and discussions carried out, the conclusions obtained are that in this study it was found that only TE waves with modes 10, 20, 01, and 11 can only propagate in the microwave room. The cutoff frequencies for each mode are 6.58 GHz, 13.19 GHz, 14.81 GHz, and 16.22 GHz. The simulation carried out produces a wave propagation profile of the TE. In modes 10 and 01 the resulting standing wave pattern has a direction of propagation that is perpendicular to the z-axis. While in modes 20 and 11 the standing wave pattern propagates parallel to the z-axis direction. The highest electric fields obtained from modes 10, 20, 01, and 11 are respectively $5.81 \times 10^6$ V/m, $6.14 \times 10^6$ V/m, $7.17 \times 10^6$ V/m, and $7.23 \times 10^6$ V/m. The plasma formed is in modes 20, 01, and 11.

## REFERENCES

[1] Brandenburg, R., Bogaerts, A., Bongers, W., Fridman, A., Fridman, G., Locke, B. R., Miller, V., Reuter, S., Schiorlin, M., Verreycken, T., & Ostrikov, K. (2019). White paper on the future of plasma science in environment, for gas conversion and agriculture. *Plasma Processes and Polymers*, **16**(1), 1700238.

[2] Van Compernolle, B., An, X., Bortnik, J., Thorne, R. M., Pribyl, P., & Gekelman, W. (2015). Excitation of chirping whistler waves in a laboratory plasma, *Physical Review Letters*, **114**.

[3] Dou, S., Tao, L., Wang, R., El Hankari, S., Chen, R., & Wang, S. (2018). Plasma-assisted synthesis and surface modification of electrode materials for renewable energy. *Advanced Materials*, **30**(21), 1705850.

[4] Sun, J., Wang, W., Yue, Q., Ma, C., Zhang, J., Zhao, X., & Song, Z. (2016). Review on microwave–metal discharges and their applications in energy and industrial processes. *Applied Energy*, **175**, 141–157.

[5] Darny, T., Pouvesle, J. M., Puech, V., Douat, C., Dozias, S., & Robert, E. (2017). Analysis of conductive target influence in plasma jet experiments through helium metastable and electric field measurements. *Plasma Sources Science and Technology*, **26**(4), 045008.

[6] Han, Z., Cai, M. J., Cheng, J. H., & Sun, D. W. (2018). Effects of electric fields and electromagnetic wave on food protein structure and functionality: A review. *Trends in Food Science and Technology*, **75**, 1–9.

[7] Schaper, L., Stalder, K. R., & Graham, W. G. (2011). Plasma production in electrically conducting liquids. *Plasma Sources Science and Technology*, **20**(3), 034004.
[8] Huang, S., Fan, Q., Xu, C., Wang, B., Wang, J., Yang, B., Tian, C., & Meng, Z. (2020). A visible-light-transparent camouflage-compatible flexible metasurface for infrared–radar stealth applications. *Journal of Physics D: Applied Physics*, **54**(1), 015001.
[9] Consoli, F., De Angelis, R., Duvillaret, L., Andreoli, P. L., Cipriani, M., Cristofari, G., Di Giorgio, G., Ingenito, F., & Verona, C. (2016). Time-resolved absolute measurements by electro-optic effect of giant electromagnetic pulses due to laser-plasma interaction in nanosecond regime. *Scientific Reports*, *6*(1), 27889.
[10] Islamov, I. J., Ismibayli, E. G., Gaziyev, Y. G., Ahmadova, S. R., & Abdullayev, R. S. (2019). Modeling of the electromagnetic field of a rectangular waveguide with side holes. *Progress In Electromagnetics Research Letters*, **81**, 127–132.
[11] Tretyakov, O. A. & Erden, F. (2021). A novel simple format of Maxwell's equations in SI units. *IEEE Access*, **9**, 88272–88278.
[12] Bokil, V. A., Cheng, Y., Jiang, Y., & Li, F. (2017). Energy stable discontinuous Galerkin methods for Maxwell's equations in nonlinear optical media. *Journal of Computational Physics*, **350**, 420–452.
[13] Gratus, J., McCall, M. W., & Kinsler, P. (2020). Electromagnetism, axions, and topology: a first-order operator approach to constitutive responses provides greater freedom. *Physical Review A*, *101*(4), 043804.
[14] Kaminer, I., Bekenstein, R., Nemirovsky, J., & Segev, M. (2012). Nondiffracting accelerating wave packets of Maxwell's equations. *Physical review letters*, **108**(16), 163901.
[15] Dev, S. R., Kannan, S., Gariepy, Y., & Raghavan, V. G. (2012). Optimization of radiofrequency heating of in-shell eggs through finite element modeling and experimental trials. *Progress In Electromagnetics Research B*, **45**, 203–222.
[16] Zhu, Y., Chen, X., Yuan, W., Chu, Z., Wong, K. Y., Lei, D., & Yu, Y. (2021). A waveguide metasurface based quasi-far-field transverse-electric superlens. *Opto-Electronic Advances*, **4**(10), 210013.
[17] Husein, I. R., Nawi, N. D., & Hairi, H. M. (2021). Electrical discharge of butane and propane for carbon plasma with air impurities, slightly ionized at high pressure. *Science, Technology and Communication Journal*, **1**(3), 109–116.
[18] Yi, Z., Qiu, W., Jiao, Y., Row, K. H., Cheng, Y. D., & Jin, Y. (2021). Calculation of electric field and temperature distribution within a microwave oven with realistic geometric features geometric features using numeric simulations. *Journal of Microwave Power and Electromagnetic Energy*, **55**(1), 3–27.
[19] Rahayu, Y., & Artiyah, I. (2021). Design and development of microstrip antenna circular patch array for maritime radar applications. *Science, Technology and Communication Journal*, **1**(3), 82–86.
[20] Luan, D., Tang, J., Pedrow, P. D., Liu, F., & Tang, Z. (2016). Analysis of electric field distribution within a microwave assisted thermal sterilization (MATS) system by computer simulation. *Journal of Food Engineering*, **188**, 87–97.
[21] Savaloni, H., Savari, R., & Abbasi, S. (2018). Application of Mn nano-flower sculptured thin films produced on interdigitated pattern as cathode and anode electrodes in field ionization gas sensor. *Current Applied Physics*, **18**(8), 869–878.
[22] Aversa, R., Petrescu, R. V., Apicella, A., & Petrescu, F. I. (2016). The basic elements of life's. *American Journal of Engineering and Applied Sciences*, **9**(4), 1189–1197.
[23] Comunian, S., Dongo, D., Milani, C., & Palestini, P. (2020). Air pollution and COVID-19: the role of particulate matter in the spread and increase of COVID-19's morbidity and mortality. *International Journal of Environmental Research and Public Health*, **17**(12), 4487.
[24] Nandanwar, S. U., Corbin, D. R., & Shiflett, M. B. (2020). A review of porous adsorbents for the separation of nitrogen from natural gas. *Industrial & Engineering Chemistry Research*, **59**(30), 13355–13369.
[25] Torrisi, L., Cutroneo, M., & Torrisi, A. (2020). Laser-generated Cu plasma in vacuum and in nitrogen gas. *Vacuum*, **178**, 109422.